International Journal of Optics and Applications 2015, 5(4): 133-146
DOI: 10.5923/j.optics.20150504.04

Modeling and Analysis of a Miniaturized Ring Modulator Using Silicon-Polymer-Metal Hybrid Plasmonic Phase Shifter. Part II: Performance Predictions

Alhuda A. Al-Mfrji[1], Shelan K. Tawfeeq[1], Raad S. Fyath[2,*]

[1]Institute of Laser for Postgraduate Studies, University of Baghdad, Iraq
[2]College of Engineering, Al-Nahrain University, Iraq

Abstract The ring modulator described in part I of this paper is designed here for two operating wavelengths 1550nm and 1310nm. For each wavelength, three structures are designed corresponding to three values of polymer slot widths (40, 50 and 60nm). The performance of these modulators are simulated using COMSOL software (version 4.3b) and the results are discussed and compared with theoretical predictions. The performance of intensity modulation/direct detection short range and long rang optical communication systems incorporating the designed modulators is simulated for 40 and 100Gb/s data rates using Optisystem software (version 12). The results reveal that an average energy per bit as low as 0.05fJ can be obtained when the 1550nm modulator is designed with a phase shifter length equals twice the coupling length.

Keywords Ring modulator, Hybrid plasmonic phase shifter, Electro-Optic polymer

1. Performance of the 1550nm Modulators

This section presents simulation results for three 1550nm ring modulators designed with different polymer slot widths W_{sl} (40nm, 50nm and 60nm). The design methodology presented in Part I of this paper is used to find the corresponding values of silicon waveguide width that makes the real parts of the effective indices of the photonic mode and plasmonic mode equal and hence ensuring phase matching between the two modes. The refractive indices of silicon, silica, and silver used in the simulation are 3.48 [1], 1.44, and 0.15 + j11.5 [2], respectively. The electro-optic (EO) organic material used in the simulation is Carbazole-Phenoxy based Methacrylate homopolymer. The refractive index of the polymer is characterized by $n_{pol} = 1.63$ at zero applied voltage and an EO coefficient γ_{33} of 80 pm/V. The common geometric parameter values used to simulate the three modulators are silicon waveguide height $H_{si} = 220\text{nm}$, polymer slot height $H_{sl} = 100\text{nm}$, and height of silica space between silicon waveguide and plasmonic waveguide $S = 120\text{nm}$.

1.1. Modulator Structure Parameters Deduced from the Simulation

Table 1 lists the individual parameter values obtained via simulation for the three modulators. Few remarks about Table 1 are given here

(i) The silicon-plasmonic hybrid phase shifter behaves as a directional coupler where two eigen modes (quasi-odd and quasi-even modes) will be excited when the hybrid phase shifter is driven by the input photonic mode. The effective refractive indices of these two modes are complex and denoted here by $n_e = n_{er} + jn_{ei}$ and $n_o = n_{or} + jn_{oi}$, respectively.

(ii) The phase velocity mismatch between the photonic mode and plasmonic mode δ and the coupling constant characterizing the virtual hybrid phase shifter coupler κ are calculated using the relations $\delta = (\beta_{ph} - \beta_{plr})/2$ and $\kappa = (\beta_{er} - \beta_{or})/2$ [3] where $\beta_{ph} = k_0 n_{ph}$ is the propagation constant of the photonic mode, $\beta_{pl} = \beta_{plr} + j\beta_{pli}$ is the propagation constant of the metal-dielectric-metal (MDM) plasmonic mode (k_0 is the vacuum propagation constant). Further, the propagation constants of the quasi-even and quasi-odd modes are given, respectively, by $\beta_e = k_0\beta_e = \beta_{er} + j\beta_{ei}$ and $\beta_o = k_0\beta_o = \beta_{or} + j\beta_{oi}$.

(iii) The coupling length between the photonic and plasmonic waveguides is estimated using the relation $L_c = \pi/\left(2\sqrt{|\kappa^2| + |\delta^2|}\right)$. Note that the three modulators are characterized by $|\delta/\kappa| \ll 1$ which indicates perfect velocity match between the photon mode (in silicon waveguide) and the plasmonic mode (in the MDM waveguide).

* Corresponding author:
rsfyath@nahrain-eng.org (Raad S. Fyath)
Published online at http://journal.sapub.org/optics

Table 1. Parameter values obtained via simulation for the three 1550nm modulators

Parameters	Modulator 1 ($W_{sl} = 40nm$)	Modulator 2 ($W_{sl} = 50nm$)	Modulator 3 ($W_{sl} = 60nm$)
Silicon waveguide width W_{si} (nm)	410.0	373.0	351.8
Effective refractive index of photonic mode $n_{ph} = n_{phr}$	2.2569	2.1396	2.0585
Effective refractive index of plasmonic mode $n_{pl} = n_{plr} + jn_{pli}$	$2.2569 + j0.0094$	$2.1399 + j0.0080$	$2.0586 + j0.0071$
Effective refractive index of quasi-even mode $n_e = n_{er} + jn_{ei}$	$2.3623 + j0.0055$	$2.2576 + j0.0048$	$2.1860 + j0.0042$
Effective refractive index of quasi-odd mode $n_o = n_{or} + jn_{oi}$	$2.0181 + j0.0041$	$1.9338 + j0.0036$	$1.8269 + j0.0032$
Phase velocity mismatch δ (μm^{-1})	0	-6×10^{-4}	-2×10^{-4}
Coupling constant κ (μm^{-1})	0.5683	0.6562	0.7277
Coupling length L_c (μm)	2.76	2.39	2.15
Mean attenuation length of the hybrid waveguide L_a (μm)	52.09	60.91	69.10
Ring circumference L (μm)	29.53	29.70	30.11
Transmission coefficient between ring and bus waveguide τ	0.7926	0.8376	0.8649

(iv) The length of the hybrid phase shifter L_{ps} is set equals to $4L_c$ to ensure high transfer of power from the plasmonic mode to the photonic mode at the end of the phase shifter.

(v) The ring circumference L is set initially to $30\mu m$ in the design and then tuned slightly to ensure a resonance wavelength of 1550nm via simulation for each of the designed modulators.

(vi) The mean attenuation length of the hybrid wavelength L_a is computed as $2/\beta_{plr}$.

(vii) The simulation results reveal that the roundtrip loss of the $30\mu m$ silicon waveguide section in the racetrack is about 0.18dB. Thus the loss factor $\alpha = 10^{-0.18/20} = 0.98$. For each designed modulator, the length of the coupler section between the waveguide bus and the microring is tuned to achieve a critical coupling that satisfies $\tau_c = \alpha e^{-L_{ps}/L_a}$.

1.2. Performance Results

1.2.1. Phase Matching Condition

The phase matching between photonic and plasmonic modes is satisfied for different polymer slot widths $W_{sl}(40, 50,$ and $60nm)$ as represented by points A, B, and C in Fig. 1. The corresponding values of silicon waveguide width W_{si} are 410,373 and 351.8nm, respectively.

1.2.2. Electric Field Distribution

The electric field (Ex) profiles for photonic mode, plasmonic mode, quasi-even mode, and quasi-odd mode are depicted in Fig. 2 for the modulator designed with $W_{sl} = 50nm$. The modulator is excited by 1550nm optical signal under zero applied voltage. It can be seen that the electric fields in the plasmonic arm are much stronger than those in dielectric arm. For the quasi-even eigen mode, the electric field orientation in the two arms are the same while they become opposite in the quasi-odd eigen mode.

Figure 3 illustrates the corresponding electromagnetic energy density distribution simulated by three-dimensional (3D) finite element method (FEM) for using COMSOL software for the silicon plasmonic hybrid phaseshifter.

Figure 4 shows the energy density distribution in the hybrid phase shifter for the three designed modulators. The parameter values used in the simulation are taken from Table 1. The results are presented for zero applied voltage and ensure high power transfer from the plasmonic waveguide to the photonic waveguide at the endpoint of the phase shifter.

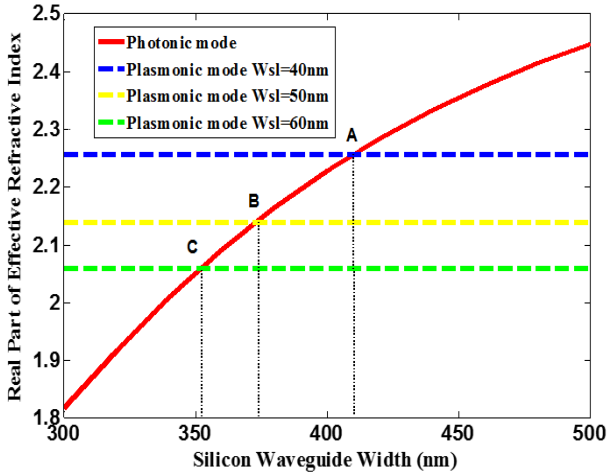

Figure 1. Real part of the effective refractive indices of photonic and plasmonic modes as a function of silicon waveguide width W_si for different polymer slot widths of 40nm, 50nm, and 60nm

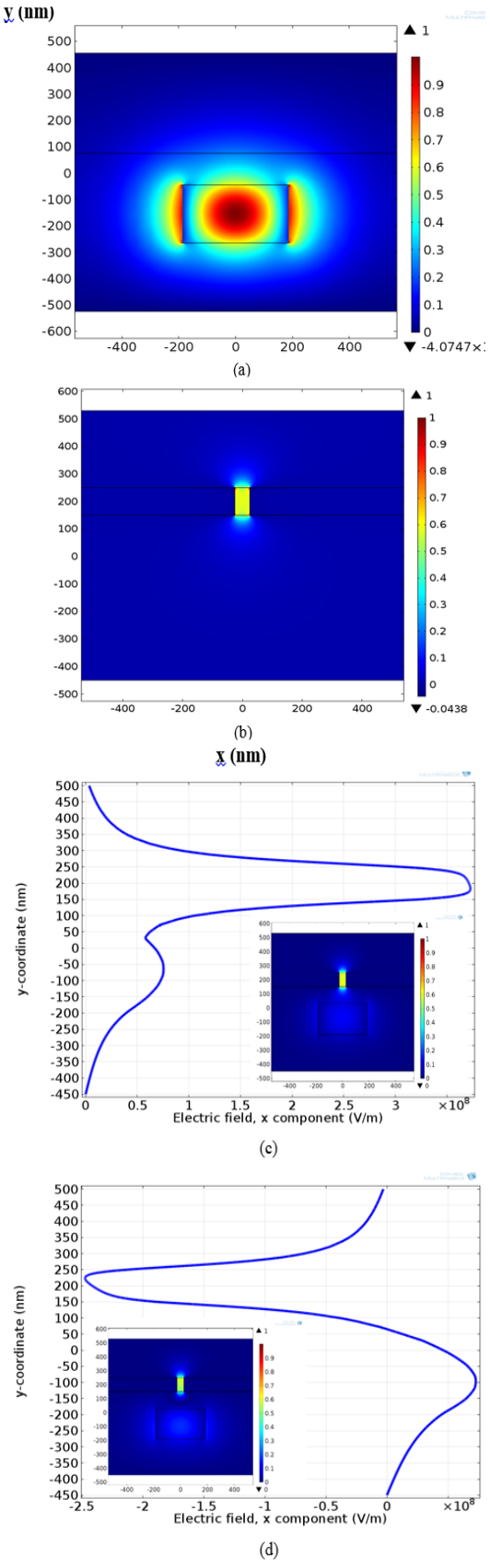

Figure 2. Electric field distribution for photonic (a), plasmonic (b), quasi-even (c), and quasi-odd (d) modes associated with $W_{sl} = 50$nm modulator operating at 1550nm and zero applied voltage

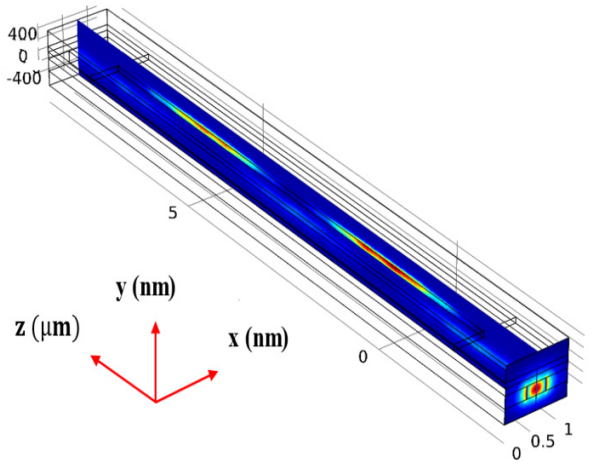

Figure 3. 3D simulated electromagnetic energy density distribution for the 50nm-width polymer slot at 1550nm photonic mode excitation

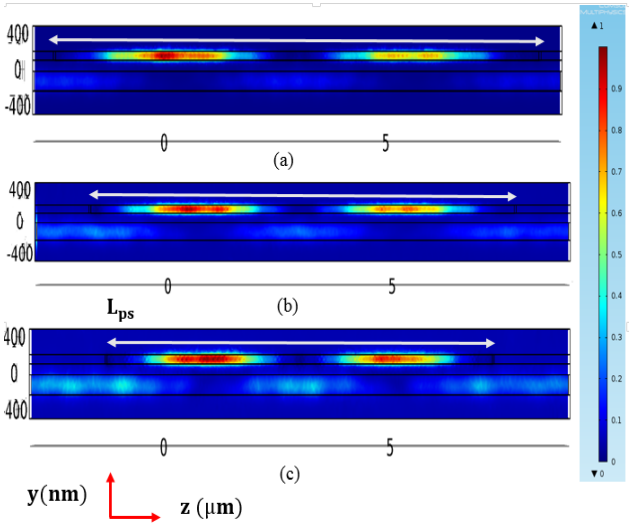

Figure 4. Energy density distribution in the hybrid phase shifter for the three modulators under zero applied voltage (a) $W_{sl} = 40$nm, (b) $W_{sl} = 50$nm, and (c) $W_{sl} = 60$nm

1.2.3. Coupling Characteristics of the Silicon-Plasmonic Coupler

Figure 5 provides clear picture for the power transfer characteristics between the silicon waveguide and plasmonic slot waveguide as a function of interaction length z (from $z = 0$ to $z = L_{ps}$, where L_{ps} is the phase shifter length). The results are presented for the three modulators under zero applied voltage. Due to the presence of losses, the variation of the power in each waveguide with propagation distance z has a damped sinusoidal behavior. As z increases, the field transfers from the silicon waveguide to the plasmonic waveguide (and vice versa) gradually owing to the interference of the quasi-even mode and quasi-odd mode. Investigating the results in this figure reveals that at $z = 4L_c$, 66%, 74%, and 78.5% of the incident power is transmitted to the of the power silicon waveguide arm when $W_{sl} = 40, 50,$ and 60nm, respectively.

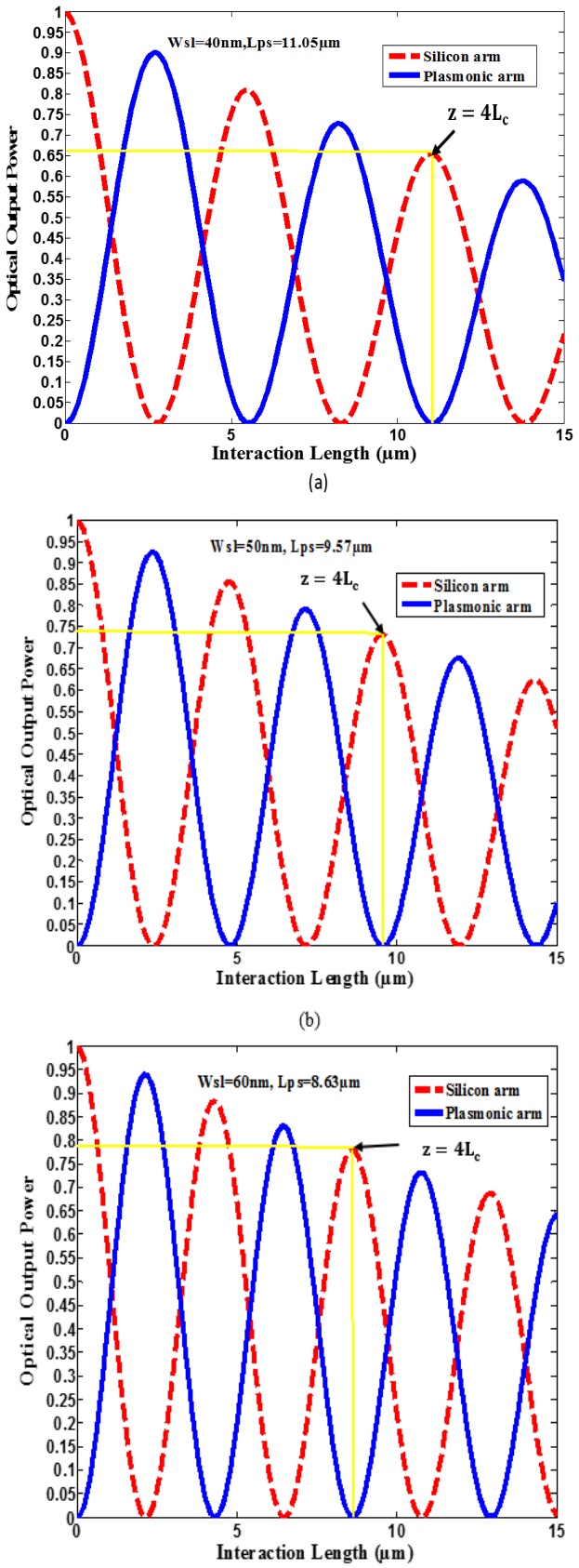

Figure 5. Dependence of output power from the two hybrid coupler arms on the interaction length z when the field is fed from the silicon arm for three modulators designed with 40 (a), 50 (b) and 60nm (c) slot widths

1.2.4. Extinction Ratio and Insertion Loss

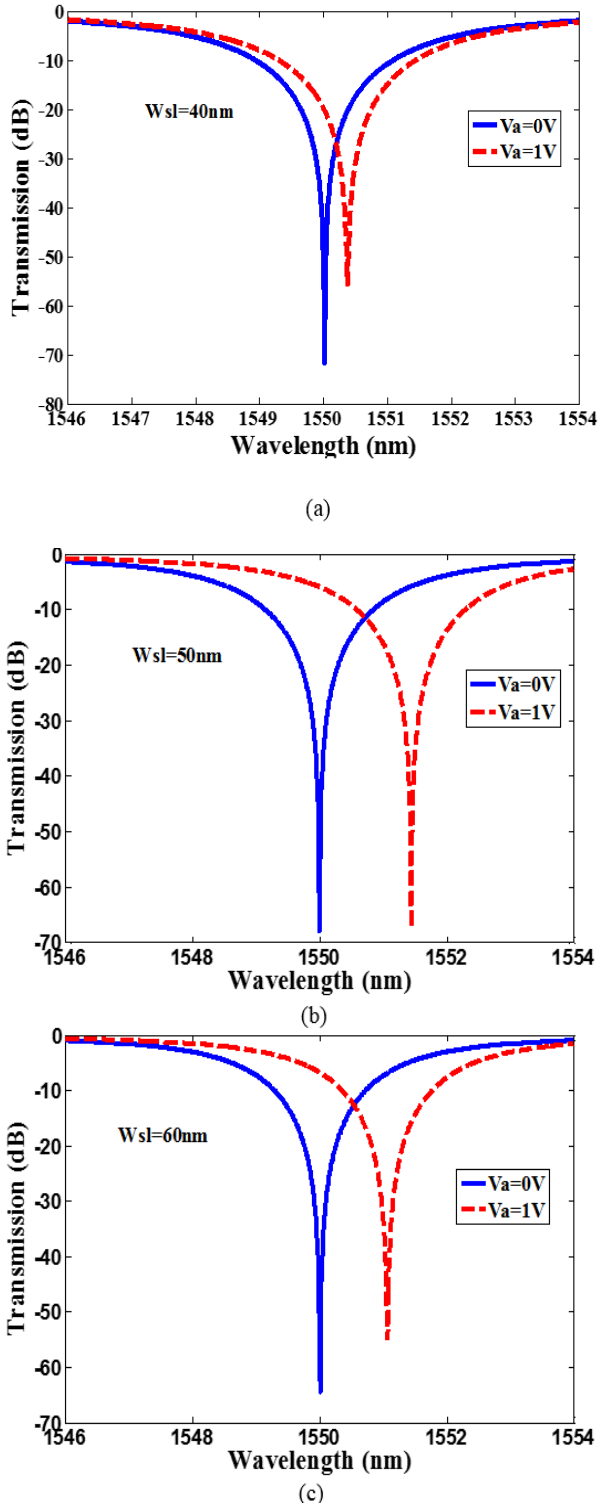

Figure 6. Transmission spectra of the three designed modulators under 0 and 1V applied voltages. (a) W_sl=40nm (b) W_sl=50nm (c) W_sl=60nm

The simulation is carried further to investigate the extinction ratio E_R and insertion loss I_L of the three ring modulators and the results are depicted in Figs. 6 and 7, respectively. Figure 6 displays the transmission characteristics versus wavelength for two values of applied

voltage V_a, 0 and 1V. Note that the 1V-applied voltage shifts the resonance frequency from 1550nm to 1550.38nm, 1550.23nm, and 1550.18nm (red shift) for the 40nm, 50nm, and 60nm slot width modulators, respectively. The corresponding extinction ratio (insertion loss) are 51.4dB (20.0dB), 46.0dB (21.8dB), 41.0dB (230.5dB), respectively.

Figures 7a and 7b examine the extinction ratio and insertion loss as function of applied voltage, respectively, for the three modulators. These metrics are very important to characterize the modulator. Note that both E_R and I_L are almost symmetric around zero voltage. An extinction ratio of 30dB is achieved when $|V_a| \approx 0.4V$ for three modulators.

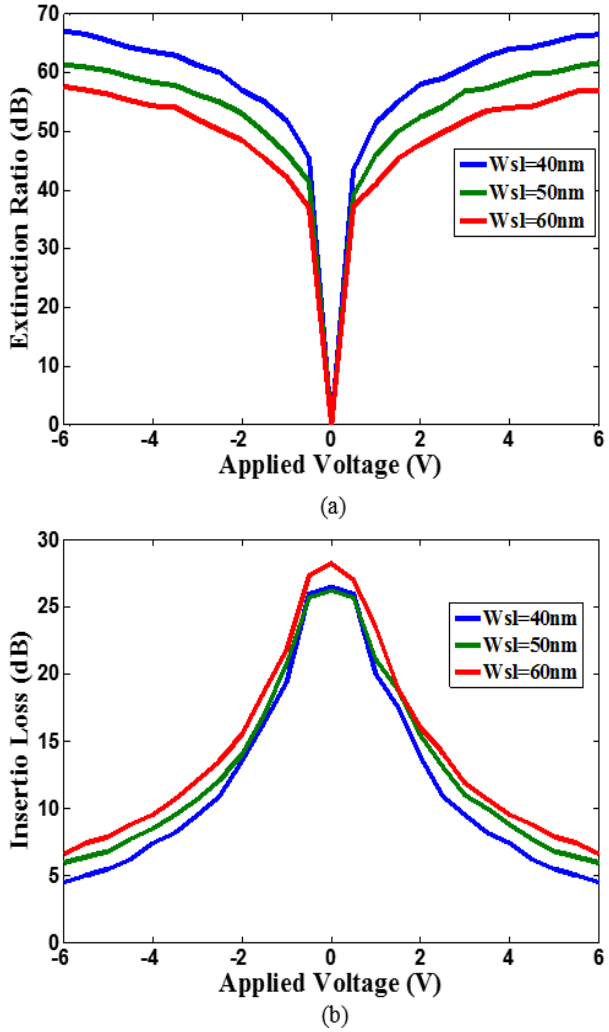

Figure 7. Extinction ratio (a) and insertion loss (b) as a function of the applied voltage for the three 1550nm modulators

1.2.5. Performance Comparison of the Designed Modulators

The performance of three modulators are compared and results are summarized in Table 2. Performance parameters that depends on the applied voltage is calculated at $V_a = 1V$. Investigating the results in this table highlights the following findings

(i) The three modulators are characterized by high extinction ratio (more than 40dB). Recent experimental demonstration of high bit rate optical communication systems indicate that optical modulators with extinction ratio as low as 20dB satisfy the requirement [4-6].

(ii) Bandwidth due to photon life time B_{plt} dominates the modulator bandwidth. The modulator bandwidth is 485, 523, and 561 GHz for slot width 40, 50, and 60nm, respectively. Note that the three modulators are designed with almost the same value of $L\,(30\,\mu m)$. Therefore, the decrease in modulator bandwidth comes from the effect of the critical coupling τ_c (see eqn. (57b) in Part I of this paper).

(iii) The average dissipated energy per bit $(\overline{E}_D)_{bit}$ decreases with increasing W_{sl}. According to eqn. (60) given in Part I of this paper, $(\overline{E}_D)_{bit}$ is directly proportional to the modulator capacitor. For the three modulators under investigation, the energy per bit is proportional to (L_{ps}/W_{sl}) since the slot height is the same for three devices. Note further L_{ps} decreases slightly as W_{sl} increases (see Table 1). Thus assuming that $(\overline{E}_D)_{bit}$ depends linearly only on $(1/W_{sl})$ will slightly under estimate the modulation bandwidth.

(iv) Theoretical predictions are in good agreement with simulation results.

1.2.6. Effect of Phase Shifter Length

In the previous subsections, the simulation results have been presented for ring modulators designed with a hybrid phase shifter having a length equals four times the coupling length (i.e., $L_{ps} = 4L_c$). In this subsection, performance comparison among ring modulators designed with different phase shifter lengths are addressed. Four modulator structures having $L_{ps} = 2L_c$, $4L_c$, $6L_c$ and $8L_c$ are designed and simulated for 1550nm operation with $W_{sl} = 50nm$. Note that the phase shifter lengths L_{ps} are even number of the coupling length in all the four structures and hence satisfy maximum power transfer for the plasmonic waveguide to the silicon waveguide at the end of the phase shifter.

Mode analysis is performed for the hybrid phase shifters in the four structures using COMSOL software and the results reveal that the modal characteristics of the plasmonic and photonic modes are not affected by the length of the phase shifter. The reason behind that is the cross section dimensions and the materials of the phase shifter structure are the same for the four modulators. The modal simulation ends with $L_c = 2.39\mu m$ and $W_{si} = 373.0nm$ for these devices.

Figure 8a-d show the field distribution in the hybrid phase shifter when $L_{ps} = 2L_c$, $4L_c$, $6L_c$ and $8L_c$, respectively. Note that when L_{ps} increases, the peak of the energy density decreases at the last part of the phase shifter due to the losses associated with the plasmonic waveguide.

For performance comparison, the four modulator structures are designed and simulated for 1550nm resonance wavelength with critical coupling between the bus and the ring. The ring circumference L is tuned slightly to

achieve 1550nm resonance wavelength. The simulation yields a ring circumference of 29.13, 29.70, 30.70, 30.27 and 30.43μm for $L_{ps} = 2L_c$, $4L_c$, $6L_c$ and $8L_c$, respectively. The corresponding critical coupling τ_c obtained via simulation is 0.9060, 0.8376, 0.7742, and 0.7156, respectively.

Table 2. Performance comparison of the three 1550nm modulators designed with different slot width

Performance parameter	Modulator 1 ($W_{sl} = 40nm$)	Modulator 2 ($W_{sl} = 50nm$)	Modulator 3 ($W_{sl} = 60nm$)	Used equations (From part I of the paper)
Average dissipated energy per bit (fJ) ($V_a = 1V$)	0.16	0.11	0.09	eqn. 53+eqn. 60
Bandwidth (due to modulator RC time constant (THz)	4.90	7.07	9.40	eqn. 53+eqn. 54
3-dB optical bandwidth (nm) (Theoritical)	4.49	4.19	3.88	eqn. 41b+eqn. 41c+eqn. 43
3-dB optical bandwidth (nm) (Simulation)	4.30	3.95	3.50	-
Bandwidth due to modulator photon life time (GHz) (Theoritical)	561.00	523.00	485.00	eqn. 41b+eqn. 41c+eqn. 58a
Bandwidth due to modulator photon life time (GHz) (Simulation)	537.00	494.00	438.00	-
Extinction ratio (dB) ($V_a = 1V$)	51.40	46.00	41.00	eqn. 63
Insertion loss (dB) ($V_a = 1V$)	20.00	21.80	23.50	eqn. 62

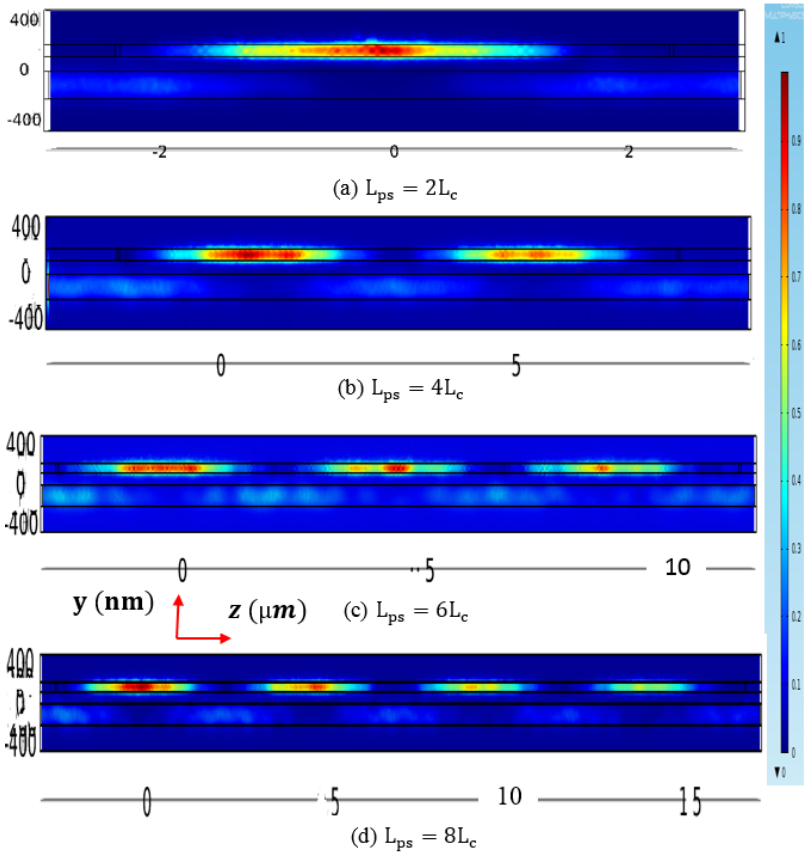

Figure 8. Energy density distribution in the hybrid phase shifter for the four modulators under zero applied voltage and $W_{sl} = 50nm$ (a) $L_{ps} = 2L_c$, (b)$L_{ps} = 4L_c$, (c) $L_{ps} = 6L_c$, and (d) $L_{ps} = 8L_c$

Table 3. Performance comparison of four 1550nm modulators designed with different phase shifter length

Performance parameter	Phase shifter length			
	$L_{ps} = 2L_c$	$L_{ps} = 4L_c$	$L_{ps} = 6L_c$	$L_{ps} = 8L_c$
Average dissipated energy per bit (fJ) ($V_a = 1V$)	0.05	0.11	0.16	0.22
Bandwidth (due to modulator RC time constant (THz)	14.14	7.07	4.71	3.53
3-dB optical bandwidth (nm)	3.10	4.18	4.42	5.20
Bandwidth due to modulator photon life time (GHz)	387.09	522.67	551.95	649.34
Extinction ratio (dB) ($V_a = 1V$)	43.40	46.00	48.89	51.90
Insertion loss (dB) ($V_a = 1V$)	18.40	21.80	21.95	22.00

Table 3 lists the main performance parameters of the four structures under investigations. These results can be explained by noting that increasing the phase shifter length will increase both cavity loss and modulator capacitance (the latter is directly proportional toL_{ps}). Investigating the results in Table 3 highlights the following findings

(i) The insertion loss is almost independent of phase shifter length and this effect is more pronounced when $L_{ps} > 2L_c$.

(ii) The extinction ratio increases slightly ($\cong 6\%$) as the phase shifter length increases by $2L_c$.

(iii) The bandwidth due to modulator RC time constant B_{RC} is inversely proportional to the phase shifter length. Note that B_{RC} is inversely proportional to modulator capacitance and hence inversely proportional to the phase shifter length.

(iv) The average dissipated energy per bit $(\overline{E}_D)_{bit} \cong 0.25CV_a^2$ increases linearly with L_{ps} due to the modulator capacitance effect. $(\overline{E}_D)_{bit}$ increases from 0.05fJ to 0.22fJ as L_{ps} increases from $2L_c$ to $8L_c$.

(v) The cavity photon lifetime decreases with increasing L_{ps} due to the increase of associated loss. Therefore, the bandwidth due to photon lifetime increases with increasing L_{ps}. B_{plt} increases from 387GHz to 649GHz as L_{ps} increases from $2L_c$ to $8L_c$.

2. Performance of 1310nm Ring Modulator

Three ring modulators are designed for 1310nm operation using different polymer slot widths (40, 50, and 60nm). The refractive indices of silicon, silica, and silver at 1310nm are set to 3.5193 [1], 1.44621 and 0.09+j8.828 [2]. Unfortunately, the refractive index and EO coefficient of Carbazole-Phenoxy based Methacrylate homopolymer are not reported in the literature at 1310nm wavelength. Therefore, the same values adopted in the 1550nm design are used here. It is worth to mention here that the EO coefficient γ_{33} of polymers generally increases when wavelength decreases [7, 8]. The values of geometric parameters that are common for the three structures are silicon waveguide height $H_{si} = 220nm$, polymer slot height $H_{sl} = 100nm$, and the height of silica space between silicon waveguide and plasmonic waveguide $S = 120nm$. Thevalues of these three dimensions are identical to those used in the 1550nm design.

The ring circumference L and the transmission coefficient between the bus waveguide and the ring τ are tuned to achieve 1310nm resonance wavelength and critical coupling, respectively, for each designed modulators. Table 4 lists the geometric and physical parameters obtained via simulation when the phase shifter length L_{ps} equals four times the coupling length L_c. Performance parameters of the modulators are summarized in Table 5. The results in the table highlights the following findings

(i) For a specific value of polymer slot widthW_{sl}, the ratio $(W_{si})_{1310nm}/(W_{si})_{1550nm} \approx 0.8$ for three values of W_{si} considered here (40, 50, and 60nm). Note the ratio between the two wavelengths is $1310/1550 = 0.845$. Thus the normalized silicon waveguide width W_{si}/λ_o is almost the same for both operating wavelengths when W_{sl} is fixed. It is worth to mention here that in microwave and millimeter wave engineering, the geometric dimensions of the designed devices are usually expressed in a normalization form with respect to wavelength. This is useful to obtain a universal design which can be configured according to the required operating wavelength. This statement seems to be also applicable for the designed modulators where W_{si} scales with wavelengths ratio. However, the effective

wavelength ratio $r_{eff} = 0.8$ rather than 0.845 since the other silicon waveguide dimensions are kept the same for both wavelength designs.

(ii) Recall that the coupling length $L_c = \lambda_o/(2|n_{er} - n_{or}|)$. At fixed value of W_{sl}, the ratio $(n_{er} - n_{or})_{1310\,nm}/(n_{er} - n_{or})_{1550\,nm}$ is approximately around $0.64 = r_{eff}^2$. This leaves $(L_c)_{1310\,nm}/(L_c)_{1550\,nm} \approx 1/r_{eff} = 1.25$ which is good agreement with results reported in the table.

(iii) Since the modulators are designed with$L_{ps} = 4L_c$, then $(L_{ps})_{1310\,nm}/(L_{ps})_{1550\,nm} = 1.25$. The modulator capacitance will increase by the same ratio, $(C_m)_{1310\,nm}/(C_m)_{1550\,nm} = 1.25$. This yields an increase in the average energy per bit and a decrease in the modulator bandwidth due to RC time constant by 1.25 when one moves from 1550nm to 1310nm design.

(iv) The quality factor $Q_o = \lambda_o/\Delta\lambda$ does not vary much for the two modulators designed at 1310nm and 1550nm resonance wavelength when W_{sl} is fixed (see Table 6). This leaves the modulator bandwidth due to photon lifetime $B_{plt} = c/(Q_o\lambda_o)$ is determined mainly by λ_o. Thus $(B_{plt})_{1310\,nm}/(B_{plt})_{1550\,nm} \approx 1550/1310 = 1.18$. This is in accord with average ratio of 1.2 estimated from both simulated and calculated bandwidth values, listed in Tables 2 and 5.

(v) The 1310nm modulators are characterized by relatively lower extinction ratio and insertion loss compared with the 1550nm counterpart.

Table 4. Parameter values obtained via simulation for the three 1310 nm modulators

Parameters	Modulator 1 ($W_{sl} = 40$nm)	Modulator 2 ($W_{sl} = 50$nm)	Modulator 3 ($W_{sl} = 60$nm)
Silicon waveguide width W_{si} (nm)	322.40	293.60	277.00
Effective refractive index of photonic mode $n_{ph} = n_{phr}$	2.3530	2.2243	2.1348
Effective refractive index of plasmonic mode $n_{pl} = n_{plr} + jn_{pli}$	$2.3531 - j0.0087$	$2.2242 - j0.0074$	$2.1349 - j0.0066$
Effective refractive index of quasi-even mode $n_e = n_{er} + jn_{ei}$	$2.4323 - j0.0047$	$2.3147 - j0.0041$	$2.2340 - j0.0036$
Effective refractive index of quasi-odd mode $n_o = n_{or} + jn_{oi}$	$2.2447 - 0.0040$	$2.0947 - j0.0035$	$1.9873 - j0.0031$
Phase velocity mismatch δ (μm^{-1})	-2.5×10^{-4}	2.5×10^{-4}	2.5×10^{-4}
Coupling constant κ (μm^{-1})	0.4499	0.5287	0.5927
Coupling length L_c (μm)	3.49	2.97	2.65
Mean attenuation length of hybrid waveguide L_a (μm)	47.92	56.34	63.17
Ring circumference L (μm)	30.62	30.62	30.68
Transmission coefficient between ring and bus waveguide τ	0.7322	0.7933	0.8283

Table 5. Performance comparison of the three 1310nm modulators designed with different slot widths

Performance parameter	Modulator 1 ($W_{sl} = 40$nm)	Modulator 2 ($W_{sl} = 50$nm)	Modulator 3 ($W_{sl} = 60$nm)
Average dissipated energy per bit (fJ) ($V_a = 1$V)	0.20	0.14	0.10
Bandwidth (due to modulator RC time constant (THz)	3.87	5.68	7.64
3-dB optical bandwidth (nm) (Theoritical)	4.32	3.55	3.05
3-dB optical bandwidth (nm) (Simulation)	4.00	3.35	3.00
Bandwidth due to modulator photon life time (GHz) (Theoritical)	755.00	621.00	533.72
Bandwidth due to modulator photon life time (GHz) (Simulation)	700.00	590.00	524.45
Extinction ratio (dB) ($V_a = 1$V)	43.40	42.90	40.10
Insertion loss (dB) ($V_a = 1$V)	18.70	20.00	22.00

Table 6. Comparison between theoretical and simulated quality factors for 1310nm and 1550nm modulators

Slot Width	Quality factor			
	1550nm modulator		1310nm modulator	
40nm	Theoritical	303.24	Theoritical	345.21
	Simulation	327.50	Simulation	360.47
50nm	Theoritical	369.01	Theoritical	369.93
	Simulation	391.05	Simulation	392.4
60nm	Theoritical	429.51	Theoritical	399.48
	Simulation	436.67	Simulation	442.86

3. Performance of Optical Communication Systems Incorporating the Designed Modulators

The aim of this section is to address the performance of short-reach and long-reach intensity modulation/direct detection (IM/DD) optical communication systems incorporating the designed ring modulators. The intensity modulation uses the electrical signal (information) to modulate the optical carrier at the transmitter while direct detection uses a photodiode to recover the information from the received modulated carrier without using local laser at the receiver side. Recently, there is increasing interest to use IM/DD technique in optical networks. For example, to provide ever-increasing user rates at limited costs of infrastructure deployment, IM/DD systems coupled with the use of a single-mode fiber (SMF) widely installed all around the orderare preferred [9]. Further, for short-reach 100Gb/s applications, IM/DD is seen as more practical than coherent modulation/detection techniques implemented in long-haul optical communication systems [10]. High bit rate IM/DD short reach communication has been demonstrated successfully at both 1550nm [11, 12] and 1310nm [13, 14]. The 1550nm and 1310nm corresponds to minimum loss wavelength and zero-dispersion wavelength of standard SMF.

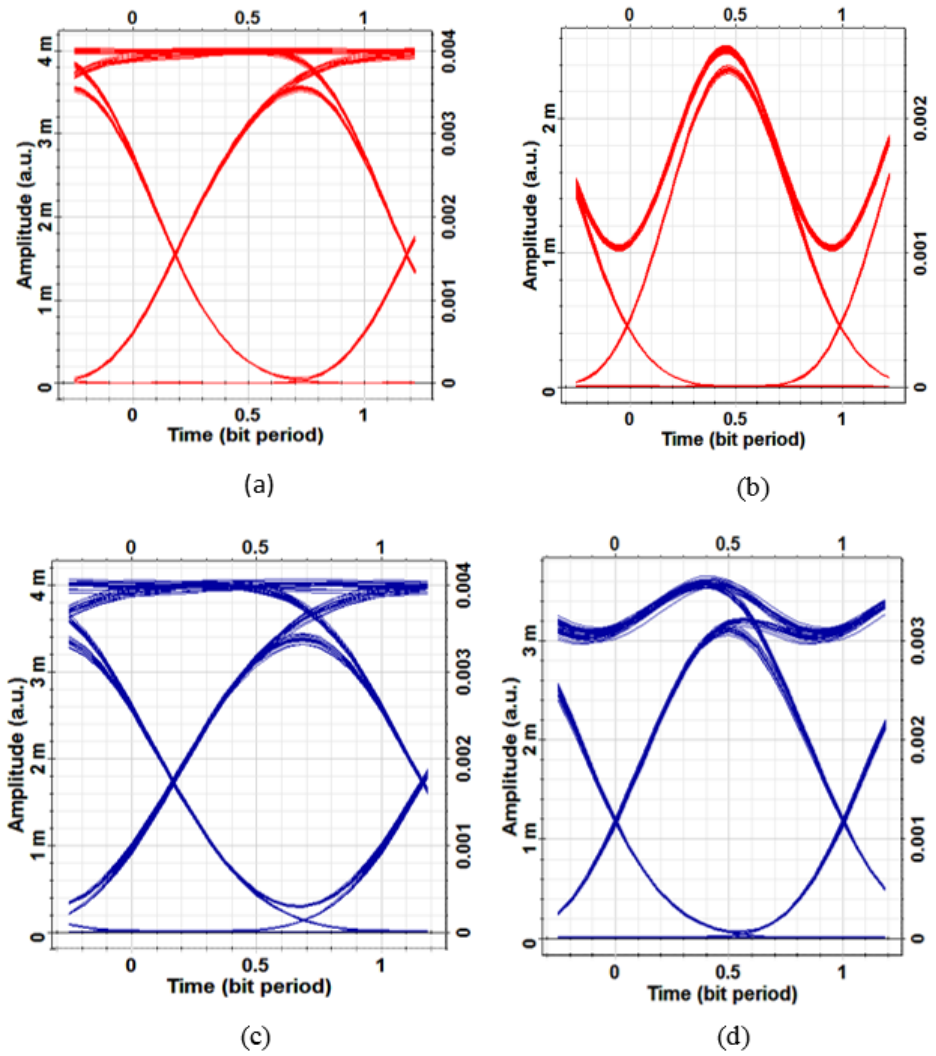

Figure 9. Transmitter eye diagrams at 1550 nm operation for 40 Gb/s NRZ (a), 40 Gb/s RZ (b), 100 Gb/s NRZ(c), and 100 Gb/s RZ (d)

The simulation results represented in this section are obtained using Optisystem ver. 12 which is a commercially software package used to simulate optical communication systems. The results are given for 1310nm and 100Gb/s IM/DD binary communication system operating as a single channel at 1550nm or 1310nm. Electronic modulator driving circuits that support binary 40Gb/s modulation have been already being used in installed high speed optical communication systems [15, 16]. However, extensive research are going on different international laborites to design electronic systems to support 100Gb/s operation [17].

To reflect the effect of the three modulator bandwidth components into the simulation, the binary data is passed through a three-stage of a first-order RC filter. Each filter uses a 50Ω resistance with a capacitance calculated to yield the required bandwidth component according to $C = 1/[2\pi R \times \text{bandwidth(Hz)}]$. The bandwidth of the driving circuit is set equal to 0.75 of the bit rate.

Figures 9a and 9b show the transmitter eye diagrams corresponding to 40Gb/s nonreturn-to-zero (NRZ) and 50% return-to-zero (RZ) signaling, respectively, at 1550nm operation. Results related to 100Gb/s are given in Figs. 9c and 9d. No DC (bias) voltage is applied to the modulator while the binary data voltage is 0V for logic Zero and 1V for logic One.

The results in Fig. 9 also reflect the behavior at 1310nm since no fiber is used in these simulation results.

Table 7. Parameter values used in OptiSystem simulation

Component	Parameter	Value
Transmitter	Wavelength (nm)	1550
	Input power (mW)	1
Single-mode fiber (SMF)	2nd-order dispersion D_{SMF} $(ps/(nm.km))$	17
	Loss α_{SMF} (dB/km)	0.2
	Dispersion slope $(ps/(nm^2.km))$	0.08
	Differential polarization group delay (ps/km)	0.2
	Effective area (μm^2)	93
	Nonlinear refractive index coefficient (m^2/W)	30×10^{-10}
	Length L_{SMF} (km)	80
Dispersion compensated fiber (DCF)	2nd order dispersion D_{DCF} $(ps/(nm.km))$	-85
	Loss α_{DCF} (dB/km)	0.5
	Dispersion slope $(ps/(nm^2.km))$	0.08
	Differential polarization group delay (ps/km)	0.2
	Effective area (μm^2)	23
	Nonlinear refractive index coefficient (m^2/W)	30×10^{-21}
	Length L_{DCF} (km)	16
Optical amplifier (OA)	Gain of the first amplifier (dB)	16
	Gain of the second amplifier (dB)	8
	Noise figure (dB)	6
Receiver	Receiver amplifier load resistance (Ω)	50
	Receiver amplifier noise figure (dB)	3
	Thermal noise power spectral density (W/Hz)	2.21×10^{-24}

3.1. Long-Reach Optical Communication System

In general, this communication system relies heavily on the deployed long-haul optical communication links and operates at 1550nm. The dispersion and losses of these links are generally compensated using dispersion compensated fibers (DCFs) and optical amplifiers (OAs), respectively. Figure 10 shows a block diagram for the long-reach optical communication system under investigation. The link consists of N identical spans. Each span contains a 80km SMF, with $17\,\mathrm{ps/(nm.km)}$ 2^{nd}-order dispersion (D_{SMF}) and $0.2\,\mathrm{dB/km}$ loss (α_{SMF}), and a 16km DCF having dispersion $D_{DCF} = -85\,\mathrm{ps/(nm.km)}$ and loss $\alpha_{DCF} = 0.5\,\mathrm{dB/km}$. Note that the average 2^{nd}-order dispersion of the span $D_{span} = (D_{SMF}L_{SMF} + D_{DCF}L_{DCF})/(L_{SMF} + L_{DCF}) = 0$ which indicates that the span is dispersionally compensated. (Here L_{SMF} and L_{DCF} are lengths of the SMF and DCF sections, respectively). An optical amplifier is also inserted after each fiber section to compensate its losses and hence spans with zero average loss are obtained. An optical bandpass filter, with optical bandwidth equals twice the receiver electrical bandwidth, is also inserted at the end of the transmission link to reduce the amount of accumulated amplified spontaneous emission generated by optical amplifiers that incident at the photodiode. An optical amplifier is also placed right of the modulator which acts as a power booster amplifier to compensate the modulator losses. Other parameter values used in the simulation are listed in Table 7.

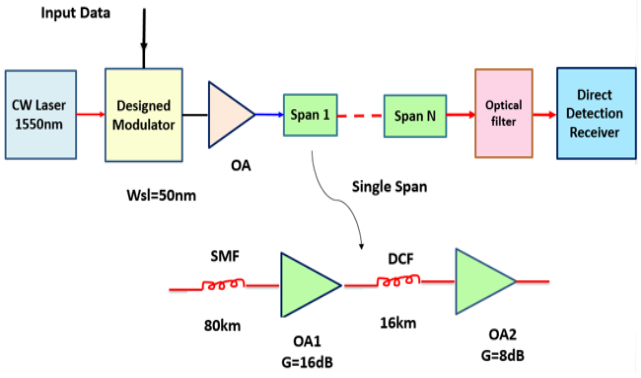

Figure 10. Long-reach optical communication system. The insert gives the components of a single span

Figures 11a-d show the variation of the bit error rate (BER) with number of spans for 40Gb/s NRZ, 40Gb/s RZ, 100Gb/s NRZ, and, 40Gb/s RZ signaling, respectively. The inserts in these figures illustrate the receiver eye diagrams at different number of spans. To achieve a BER$< 10^{-9}$, the number of spans N should be less than 9, 11, 5, and 4, respectively.

3.2. Short-Reach Optical Communication System

This subsection examines the performance of a short-reach system incorporates the designed modulators along with a SMF connecting the transmitter with receiver. From cost point of view, no DCF or OA is used to compensate the fiber dispersion and link losses, respectively.

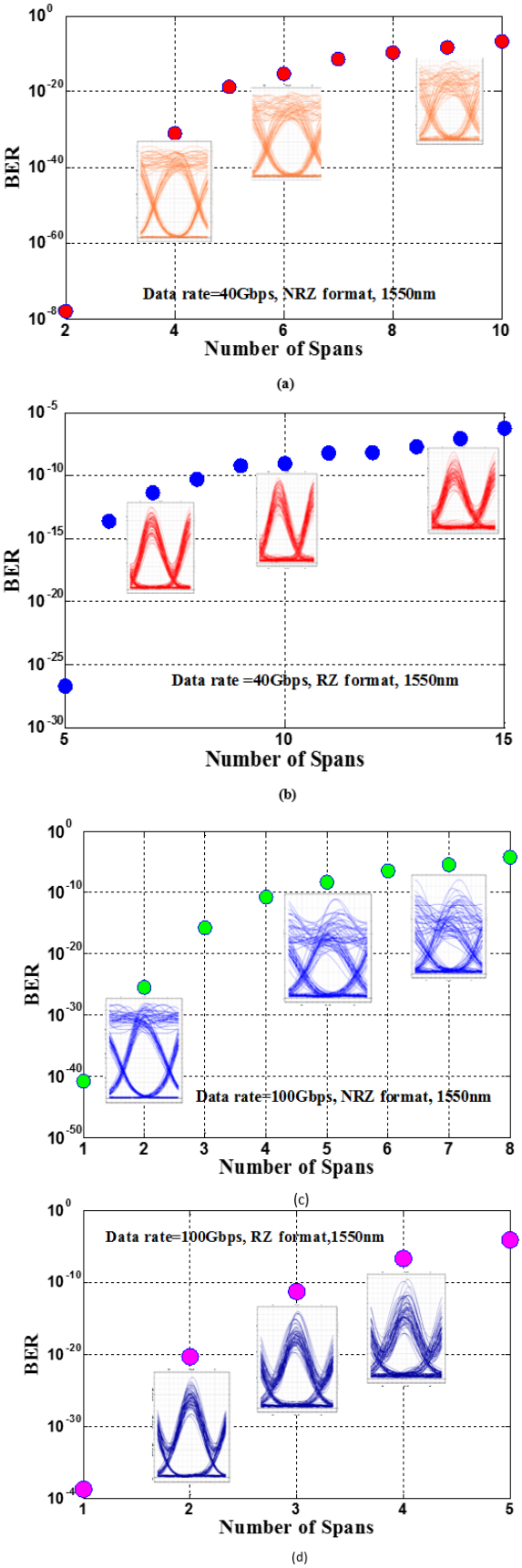

Figure 11. Dependence of BER on number of spans for 40Gb/s NRZ (a), 40Gb/s RZ (b), 100Gb/s NRZ (c), and 100Gb/s RZ (d)

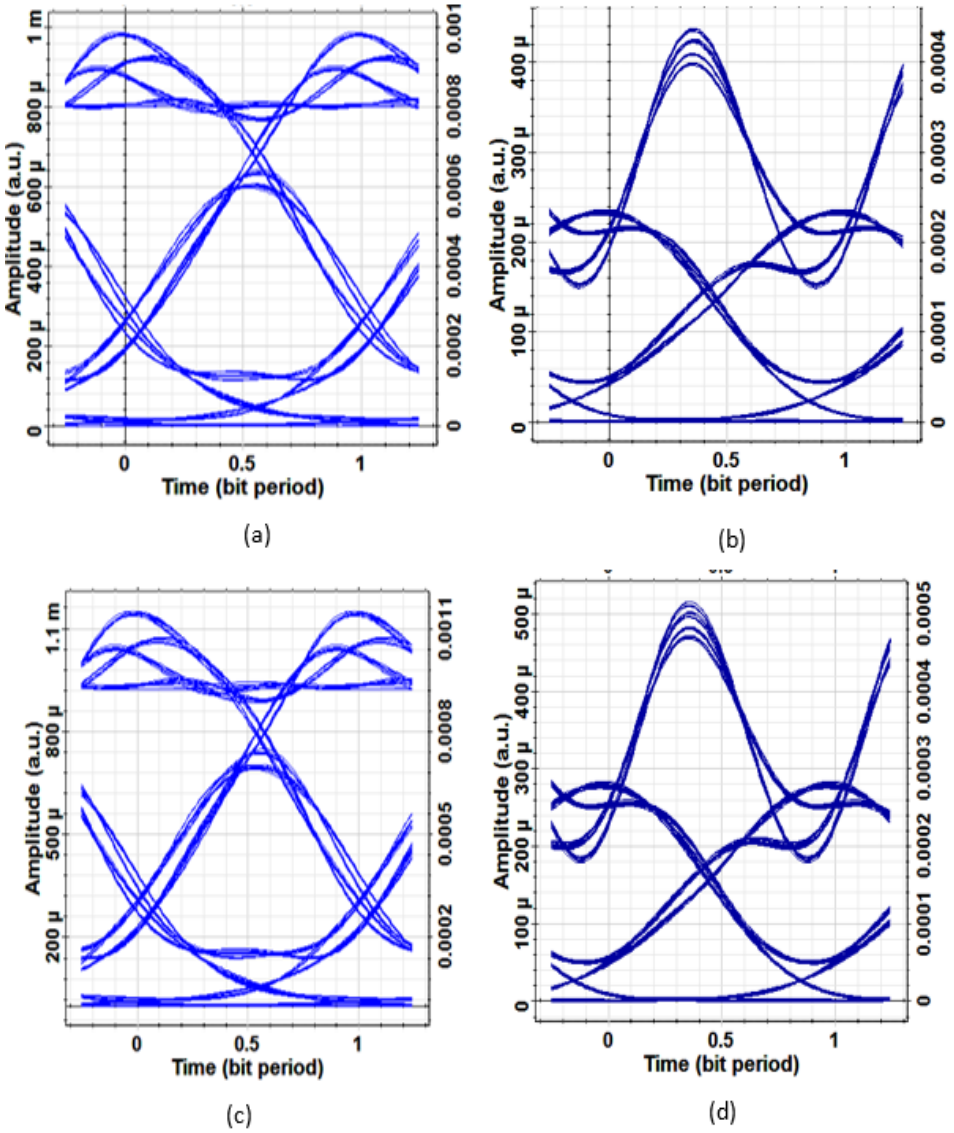

Figure 12. Receiver eye diagrams for 1550nm short-reach operation with 40Gb/s NRZ (a), 40Gb/sRZ (b), 100Gb/sNRZ (c), and 100Gb/s RZ (d)

Two modulators are considered in the simulation, one is designed for 1550nm operation and the other for 1310nm operation, both with slot width=50nm. At the 1310nm, the second-order dispersion of the SMF is approximately zero and therefore one should take the effect of the third-order dispersion through the dispersion slope $\equiv \partial D/\partial\lambda$.

Table 8 lists the maximum allowable transmission distance that yields a BER$\leq 10^{-9}$. Results are reported for 40 and 100Gb/s bit rates, NRZ and RZ signal format, and 1550 and 1310nm operation.

The receiver eye diagrams corresponding to maximum transmission lengths of these signal formats are given in Figs. 12 and 13. As expected, much longer transmission length can be obtained at 1310nm compared with 1550nm operation due to the negligible fiber second-order dispersion at 1310nm. Note that using RZ format reduces the maximum transmission length to approximately 0.77(0.87) of the NRZ length at 100Gb/s (Gb/s), respectively.

Table 8. Maximum allowable transmission length corresponding to BER $\leq 10^{-9}$ in short reach optical communication system

Wavelength	Maximum distance for BER $\leq 10^{-9}$ (km)			
	Bit rate= 40 Gb/s		Bit rate= 100 Gb/s	
	NRZ	RZ	NRZ	RZ
1550nm	4.75	3.7	0.78	0.59
1310nm	57.7	50.6	52	44.5

Note further, the ratio between the maximum transmission length at 100Gb/s to that at 40Gb/s is equal approximately to 0.16 and 0.86 at 1550nm and 1310nm, respectively, and these results are almost independent of signaling formats.

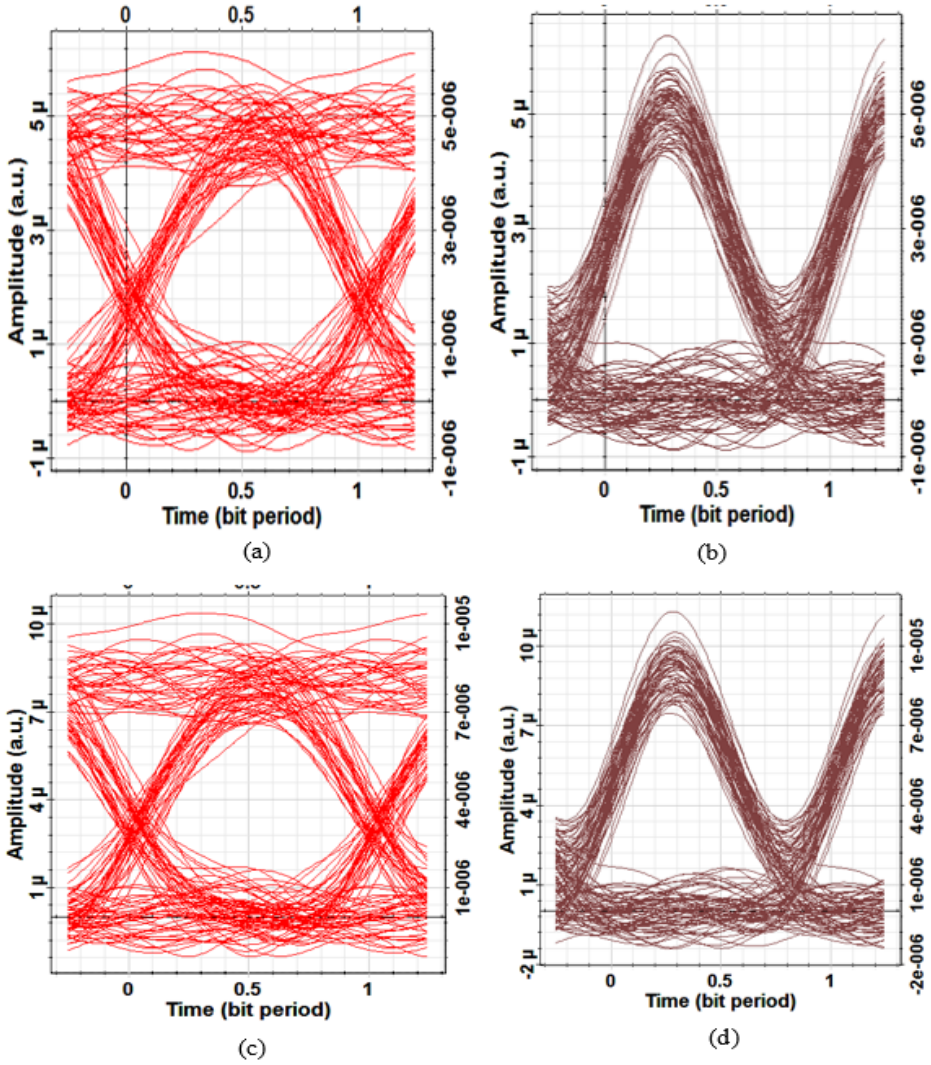

Figure 13. Receiver eye diagram for 1310nm short-reach operation with 40Gb/s NRZ (a), 40Gb/s RZ (b), 100Gb/s NRZ (c), and 100Gb/s RZ (d)

4. Conclusions

Performance predictions have been presented for plasmonic ring modulators designed for 1550nm and 1310nm wavelengths. The key role played by polymer slot width and the length of the hybrid phase shifter have been identified in detail. An extinction ratio more than 40dB is obtained at 1V applied voltage for both operating wavelengths. The average energy per bit is about 0.05fJ(0.1fJ) when the 1550nm (1310nm) modulator is designed with phase shifter length equals two times the coupling length of the virtual hybrid coupler covering the interaction between photonic mode and plasmonic mode in the phase shifter.

ACKNOWLEDGMENTS

The authors would like to thank the anonymous reviewers for their valuable comments and suggestions to improve the quality of the paper. The work is a part of a PhD research program in the Institute of Laser for Postgraduate Studies, University of Baghdad, Iraq. One of the authors, Mrs. Al-mfrji, wishes to thank the College of Engineering at Al-Nahrain University, Baghdad, Iraq, for offering her the PhD scholarship.

REFERENCES

[1] E. D. Palik, "Handbook of optical constants of solids," Orlando, FL, USA: Academic, PP. 753-763, 1985.

[2] P. B. Johnson and R. W. Christy, "Optical constants of the noble metals," Physics Review. B, Vol. 6, No. 12, PP. 4370-4379, December 1972.

[3] Q. Li and M. Qiu, "Structurally-tolerant vertical directional coupling between metal-insulator-metal plasmonic waveguide and silicon dielectric waveguide," Optics Express, Vol. 18, No. 15, PP. 15531-15543, July 2010.

[4] K. Kikuchi, H. Nosaka, H. Yamazaki, M. Nagatani, T. Goh, K. Kurishima, and T. Saida, "Design and fabrication of mixed

electronics-optics modulator for dual-carrier QPSK generation," J. Lightwave Technology, Vol. 33, No. 15, PP. 3265-3270, August 2015.

[5] D. Patel, S. Ghosh, M. Chagnon, A. Samani, V. Veerasubramanian, M. Osman, and D. Plant, "Design, analysis, and transmission system performance of a 41 GHz silicon photonic modulator," Optics Express, Vol. 23, No. 10, PP. 14263-14287, May 2015.

[6] I. Kim, O. Vassilieva, P. Palacharla, and M. Sekiya, "Mitigation and monitoring of the impact of extinction ratio of IQ-modulator on nyquist M-QAM signals," IEEE Photonics Technology Letters, Vol. 26, No. 2, PP. 177-179, January 2014.

[7] Y. Fang, S. Qishun, Z. Ying, C. Zhuang, L. Hua, and Y. Wen, "Wavelength dependence of electro-optic coefficient in Chromophore- incorporated polymers," Chinese Physics Letters, Vol. 20, No. 7, PP. 1-5, February 2003.

[8] L. R. Dalton, P. Gunter, M. Jazbinsek, O. kwon and P. Sullivan, "Organic electro-optics and photonics, molecules, polymers, and crystals," First Edition, Ch. 3, Cambridge, 2015.

[9] M. F. Sanya, L. Djogbe, A. Vianou, and C. Aupetit, "DC-biased optical OFDM for IM/DD passive optical network systems," J. Optical Communication Network, Vol. 7, No. 4, PP. 205-214, April 2015.

[10] J. C. Cartledge and A. S. Karar, "100Gb/s intensity modulation and direct detection," J. Lightwave Technology, Vol. 32, No. 16, PP. 2809-2814, August 2014.

[11] M. Chagnon, M. Morsy, M. Poulin, C. Paquet, S. Lessard, and D. Plant, "Experimental parametric study of a silicon photonic modulator enabled 112-Gb/s PAM transmission system with a DAC and ADC," J. Lightwave Technology, Vol. 33, No. 7, PP. 1380-1387, April 2015.

[12] M. Chen, J. He, and L. Chen, "Real-time demonstration of 1024 QAM OFDM transmitter in short-reach IMDD systems," IEEE Photonics Technology Letters, Vol. 27, No. 8, PP. 824-827, April 2015.

[13] M. Morsy, M. Chagnon, M. Poulin, S. Lessard, and D. Plant, "224–Gb/s 10-km transmission of PDM PAM-4 at 1.3μm using a single intensity-modulated laser and a direct-detection MIMO DSP-based receiver," J. Lightwave Technology, Vol. 33, No. 7, PP. 1417-1424, April 2015.

[14] M. Chagnon, M. Osman, M. Poulin, C. Latrasse, J. Gagne, Y. Painchaud, C. Paquet, S. Lessard, and D. Plant, "Experimental study of 112 – Gb/s short reach transmission employing PAM formats and SiP intensity modulator at 1.3μm," Optics Express, Vol. 22, No. 17, PP. 21018-21036, August 2014.

[15] Y. Zhou, K. Smith, R. Payne, A. Lord, L. Raddatz, M. Bertolini, T. Velde, C. Colombo, E. Korkmaz, M. Fontana, and S. Evans, "1.4Tb real-time alien superchannel transport demonstration over 410km installed fiber link using software reconfigurable DP–16 QAM/QPSK," J. Lightwave Technology, Vol. 33, No. 3, PP. 639-644, February 2015.

[16] M. Huang, A. Tanaka, E. Ip, Y. Huang, D. Qian, Y. Zhang, S. Zhang, P. Ji, I. Djordjevic, T. Wang, Y. Aono, S. Murakami, T. Tajima, T. Xia, and G. Wellbrock, "Terabit/s Nyquistsuperchannels in high capacity fiber field trials using DP-16QAM and DP-8QAM modulation formats," J. Lightwave Technology, Vol. 32, No. 4, PP. 776-782, February 2014.

[17] E. Lach, W. Idler, "Modulation formats for 100G and beyond," Optical Fiber Technology, Vol. 17, No. 1, PP. 377-386, August 2011.